Published in final edited form as:

Structure. 2016 April 5; 24(4): 631–640. doi:10.1016/j.str.2016.02.007.

Acoustic Injectors for Drop-On-Demand Serial Femtosecond Crystallography

Christian G. Roessler[1,20], Rakhi Agarwal[2,14], Marc Allaire[1,16,*], Roberto Alonso-Mori[9], Babak Andi[1], José F.R. Bachega[5], Martin Bommer[13], Aaron S. Brewster[3], Michael C. Browne[9], Ruchira Chatterjee[3], Eunsun Cho[4], Aina E. Cohen[11], Matthew Cowan[1], Sammy Datwani[6], Victor L. Davidson[8], Jim Defever[9], Brent Eaton[6], Richard Ellson[6], Yiping Feng[9], Lucien P. Ghislain[6], James M. Glownia[9], Guangye Han[3], Johan Hattne[3,17], Julia Hellmich[12,13], Annie Héroux[1], Mohamed Ibrahim[13], Jan Kern[3,9], Anthony Kuczewski[1], Henrik T. Lemke[9,18], Pinghua Liu[4], Lars Majlof[6], William M. McClintock[6], Stuart Myers[1], Silke Nelsen[9], Joe Olechno[6], Allen M. Orville[1,2,19,*], Nicholas K. Sauter[3], Alexei S. Soares[1,*], S. Michael Soltis[11], Heng Song[4], Richard G. Stearns[6], Rosalie Tran[3], Yingssu Tsai[9,10], Monarin Uervirojnangkoorn[3], Carrie M. Wilmot[7], Vittal Yachandra[3], Junko Yano[3], Erik T. Yukl[7,15], Diling Zhu[9], and Athina Zouni[13]

[1]Photon Sciences Division, Brookhaven National Laboratory, Upton, NY 11973-5000, USA

[2]Biosciences Department, Brookhaven National Laboratory, Upton, NY 11973-5000, USA

[3]Physical Biosciences Division, Lawrence Berkeley National Laboratory, Berkeley, CA 94720-8177, USA

[4]Department of Chemistry, Boston University, Boston, MA 02215-2521, USA

[5]Centro de Biotecnologia Molecular Estructural, Instituto de Física de São Carlos, Universidade de São Paulo, Caixa Postal 369, São Carlos, CEP: 13560-970, Brazil

[*]Correspondence: mallaire@lbl.gov (M.A.), allen.orville@diamond.ac.uk (A.M.O.), soares@bnl.gov (A.S.S.).

[14]Present address: Department of Physical Sciences, St. Joseph's College, Patchogue, NY 11772, USA

[15]Present address: Department of Chemistry and Biochemistry, New Mexico State University, Las Cruces, NM 88003-8001, USA

[16]Present address: Molecular Biophysics and Integrated Bioimaging, Lawrence Berkeley National Laboratory, Berkeley, CA 94720-8177, USA

[17]Present address: Janelia Research Campus, Howard Hughes Medical Institute, Ashburn, VA 20147, USA

[18]Present address: Paul Scherrer Institut, 5232 Villigen PSI, Switzerland

[19]Present address: Diamond Light Source Ltd, Diamond House, Harwell Science & Innovation Campus, Didcot, Oxfordshire OX11 0DE, UK

[20]Present address: Ventana Medical Systems, Inc., Oro Valley, AZ 85755, USA

ACCESSION NUMBERS

Structure factors and atomic coordinates have been deposited with the PDB: lysozyme (PDB: 5F81), stachydrine demethylase (PDB: 5HL4), and thermolysin (PDB: 5HQD).

SUPPLEMENTAL INFORMATION

Supplemental Information includes Supplemental Experimental Procedures, three figures, and four tables and can be found with this article online at http://dx.doi.org/10.1016/j.str.2016.02.007.

AUTHOR CONTRIBUTIONS

M.A., A.S.S., and A.M.O. conceived the experiment, which was designed with C.G.R., J.Y., V.Y., R.E., J.O., H.L., and S.M.S. Samples were prepared by C.G.R., R.A., B.A., J.K., J. He., M.I., M.B., A.Z.,R, R.T., R.C., G.H., E.C., H.S., P.L., J.F.R.B., R.C.G., C.M.W., E.T.Y., V.L.D., M.A., and A.S.S. Acoustic injectors were designed by C.G.R., S.M., A.K., M.C., S.D., B.E., R.E., L.P.G., L.M., W.M.M., J.O., R.G.S., M.A., A.S.S., and A.M.O. SFX experiments were carried out by C.G.R., R.A., S.M., A.K., M.C., R.G.S., Y.T., D.Z., R.A.-M., H.L., M.A., A.S.S., and A.M.O. Beamline setup was done by Y.T., J.M.G., D.Z., J.D., Y.F., M.B., R.A.-M., S.N., and H.L. Diffraction instrumentation was calibrated and operated by Y.T., D.Z., J.D, Y.F., M.B., R.A.-M., S.N., H.L., A.C., and S.M.S. Data were analyzed by C.G.R., A.H., A.S.B., J. Ha., M.U., and N.K.S. C.G.R. and A.M.O. wrote the paper with discussion and improvements from all authors.

[6]Labcyte Inc., Sunnyvale, CA 94089, USA

[7]Department of Biochemistry, Molecular Biology & Biophysics, University of Minnesota, Minneapolis, MN 55455, USA

[8]Burnett School of Biomedical Sciences, University of Central Florida, Orlando, FL 32816-2364, USA

[9]Linac Coherent Light Source, SLAC National Accelerator Laboratory, Menlo Park, CA 94025, USA

[10]Department of Chemistry, Stanford University, Stanford, CA 94305-4401, USA

[11]Stanford Synchrotron Radiation Lightsource, SLAC National Accelerator Laboratory, Menlo Park, CA 94025, USA

[12]Max-Volmer-Laboratorium für Biophysikalische Chemie, Technische Universität, D-10623 Berlin, Germany

[13]Institut für Biologie, Humboldt-Universität zu Berlin, D-10099 Berlin, Germany

SUMMARY

X-Ray free-electron lasers (XFELs) provide very intense X-ray pulses suitable for macromolecular crystallography. Each X-ray pulse typically lasts for tens of femtoseconds and the interval between pulses is many orders of magnitude longer. Here we describe two novel acoustic injection systems that use focused sound waves to eject picoliter to nanoliter crystal-containing droplets out of micro-plates and into the X-ray pulse from which diffraction data are collected. The on-demand droplet delivery is synchronized to the XFEL pulse scheme, resulting in X-ray pulses intersecting up to 88% of the droplets. We tested several types of samples in a range of crystallization conditions, wherein the overall crystal hit ratio (e.g., fraction of images with observable diffraction patterns) is a function of the microcrystal slurry concentration. We report crystal structures from lysozyme, thermolysin, and stachydrine demethylase (Stc2). Additional samples were screened to demonstrate that these methods can be applied to rare samples.

Graphical abstract

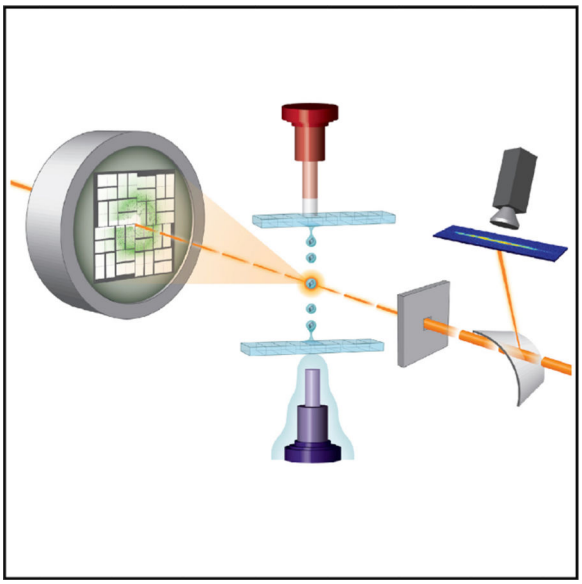

INTRODUCTION

Serial femtosecond crystallography (SFX) strategies exploit X-ray pulses from a free-electron laser (FEL) to obtain a macro-molecular structure from a slurry of nanocrystals or microcrystals (Chapman et al., 2014; Schlichting, 2015). The first sample delivery methods for SFX used liquid jets that flow a stream of microcrystalline slurry through the X-ray interaction region (Chapman et al., 2011; Sierra et al., 2012; Weierstall, 2014). More recent methods have included high viscosity extruders for lipidic cubic phase (LCP) samples (Conrad et al., 2015; Liu et al., 2013, 2014b; Sugahara et al., 2015; Weierstall et al., 2014). In these flowing-sample systems, diffraction patterns result each time a randomly oriented, diffraction quality crystal intersects an X-ray pulse (Aquila et al., 2012; Barends et al., 2014; Boutet et al., 2012; Chapman et al., 2011; Demirci et al., 2013; Johansson et al., 2013; Johansson et al., 2012; Kern et al., 2012, 2013; Liu et al., 2013; Lomb et al., 2011; Redecke et al., 2013; Sierra et al., 2012). Crystals are wasted when they pass through the interaction region when no X-rays are present. An alternative method uses fixed targets that raster and/or rotate samples through the X-ray beam (Cohen et al., 2014; Hirata et al., 2014; Hunter et al., 2014; Roedig et al., 2015; Suga et al., 2015). These latter approaches provide an opportunity to collect a series of related diffraction patterns from large, cryo-cooled crystals using a small X-ray beam and crystal translation/rotation movements between shots.

The Linac Coherent Light Source (LCLS) produces a hard X-ray pulse up to 120 times per second. If every pulse yielded usable data, then the total time to collect 50,000 images for a complete dataset would be less than 10 min. Thus, the goal of all sample delivery methods at the LCLS is to use the full 120-Hz pulse frequency such that each pulse yields usable diffraction data. To these ends, fixed target, goniometer-based approaches yield diffraction patterns on each shot. If there is a known orientation relationship between successive images, then their intensities can almost always be integrated and merged. This can result in high-quality structures from many fewer images than is typical for liquid jet-based SFX

methods, but does so at a reduced repetition rate of the instrument. For liquid jets, wherein a continuous stream of microcrystals passes at random times through the interaction region, most of the X-ray pulses do not yield suitable diffraction patterns. Under ideal conditions, about one out of 1,600 crystals in a microjet stream is exposed to an X-ray pulse and the rest are wasted (Weierstall, 2014). Therefore, increasing sample efficiency (i.e., the fraction of crystals in a sample which produce a diffraction pattern) would also extend SFX to systems that do not readily produce millions of crystals.

In this paper we present results from two injection systems based on acoustic droplet ejection (ADE) technology for delivering crystals into the LCLS X-ray beam. One acoustic injector provides optimal stability and control of the droplet, while the other is optimized for flexibility and different ejection geometries. We demonstrate drop-on-demand acoustic injection of eight protein samples into the X-ray laser in synchrony with pulses.

RESULTS

Acoustic Injectors Deliver Crystal-Containing Droplets

ADE uses the radiation pressure associated with focused sound energy to eject nanoliter to picoliter droplets with repeatable volume and velocity, typically from solutions contained in a reservoir (Ellson et al., 2003). The acoustic instrumentation does not come directly into contact with the sample, eliminating cleaning time between samples. While capillary and microfluidic devices can clog and damage crystals by subjecting them to shear force, in ADE the droplet emerges from the meniscus of the fluid without passing through an orifice. Some current applications of ADE in macromolecular crystallography (MX) include crystal growth (Villaseñor et al., 2012), microseeding (Villaseñor et al., 2010), ligand screening (Cole et al., 2014; Teplitsky et al., 2015; Yin et al., 2014), and discrete crystal deposition onto data collection media for synchrotron-based cryo-crystallography (Cuttitta et al., 2015; Heroux et al., 2014; Roessler et al., 2013; Soares et al., 2011).

We designed two acoustic injectors to deliver droplets on-demand and directly into an X-ray beam (Figure 1 and S1). One injector was based on a modified Labcyte Echo 555 instrument (Labcyte) (Aerni et al., 2005), in which the acoustic transducer assembly was moved outside the instrument case and directly beneath the X-ray beam. This modified Echo injector retained all of the capabilities of the commercial Labcyte system, including applying its Dynamic Fluid Analysis software to calibrate both the acoustic focus and acoustic toneburst power for consistent droplet volume and velocity (Supplemental Experimental Procedures). Crystal slurries were loaded into rows of wells within acoustically compatible 384-well format micro-plates. Each microplate was attached to a set of motorized translational stages with sufficient travel to position each well between the transducer and the X-ray beam. Droplets were ejected upward into the X-ray beam from the top surface of the slurry with a fixed droplet volume of 2.5 nl (~168 μm diameter for the droplet). After the sample was expended, translating the plate over to the next well was accomplished remotely in seconds and droplet ejection parameters were determined automatically for the next well.

A second injection system that used different control software and transducers was also tested (Figure 1 and Figure S1B–S1C). This system could produce several different-sized

droplets (57–168-μm diameter, corresponding to 0.1–2.5 nl, respectively) as a function of different acoustic transducers with center frequencies at 10, 15, or 25 MHz. It could also be configured to eject droplets downward into the X-ray beam, in contrast to the modified Echo system. Acoustic coupling between the transducer and the microplate was achieved through a 1% (w/v) agarose plug.

Drop-On-Demand SFX Experiments at Ambient Conditions

Our experiments were performed in air at the X-ray Pump Probe (XPP) instrument at the LCLS (Chollet et al., 2015; Moeller et al., 2011) using a 9.1-keV X-ray beam ($\Delta E = 0.03$ keV full width at half maximum [FWHM]) with pulse durations nominally at 45 fs and up to 1 mJ of power per pulse. Beryllium compound refractive lenses were used to focus the beam from 100 μm down to 30 μm (FWHM) at the interaction region. In some cases the beam was attenuated up to a factor of ten to prevent pixel overloads from high-intensity, low-angle Bragg reflections. Diffuse air-scattered X-rays were blocked by a pinhole aperture positioned 50 mm upstream of the interaction region. A Cornell-SLAC pixel array detector (CSPAD) (Hart et al., 2012) was installed 108 mm downstream of the interaction region and recorded Bragg reflections out to 1.62-Å resolution in the corners.

Drop-on-demand timing was achieved by triggering the acoustic injection pulse using the LCLS pulse clock. A tunable delay was added to account for droplet speed, distance to the X-ray interaction region from the meniscus, and deceleration due to air friction. Typical droplet speeds were on the order of 1 m s^{-1}. The distance between the interaction point with the X-rays and the sample meniscus varied between 3 and 14 mm, though longer distances could be achieved at the expense of precision in droplet trajectory. Shot-to-shot calibration of the ejection event was controlled using the on-axis camera system and an image-analysis algorithm which took the droplet position and compared it with the position of the X-ray beam up to the maximal triggered pulse rate of 60 Hz.

Acoustic Injection of Crystalline Slurries

The primary goal of these experiments was to demonstrate feasibility of on-demand droplet injection with various sample conditions at the LCLS. To this end, several test samples were injected into the X-ray beam using the acoustic injectors. They included hen-egg-white lysozyme (HEWL), thermolysin from *Bacillus stearothermophilus*, stachydrine demethylase (Stc2) from *Sinorhizobium meliloti* (Daughtry et al., 2012), the diheme enzyme MauG in complex with methylamine dehydrogenase (MADH) from *Paracoccus denitrificans* (Yukl et al., 2013), giant extracellular hemoglobin (*Glossoscol expaulistus*) (Bachega et al., 2011; Ruggiero Bachega et al., 2015), and photosystem II (PS-II) from *Thermosynechococcus elongatus* (Hellmich et al., 2014; Kern et al., 2005). These samples represent a range of protein crystallization variables typically encountered in MX experiments including unit cell dimensions, crystal size, crystal morphology, space group, solvent content, and crystallization chemistry (Supplemental Information and Table S1). All crystal samples were either in their original mother liquor or, in a few cases, the mother liquor was supplemented with 0.08%-0.2% (w/v) agarose to counter crystal settling in mother liquor (Supplemental Information).

From all of these samples a total of over 232,000 images were collected and analyzed with *cctbx.xfel* (Hattne et al., 2014), of which approximately 12,000 (5.2%) were considered crystal hits based on the presence of 15 or more Bragg peaks (Figure 2). By comparison, this is far fewer images than is typically collected for an SFX dataset with liquid jets or LCP injectors. For example, Kang et al. (2015) collected more than four million images over a 12-hr period on coherent X-ray imaging operating at 120 Hz, with an LCP injector, from which they reported 22,262 crystal hits (~0.45%) and 18,874 indexed lattices (85%) that contributed to the 3.3-Å structure. However, our XPP beamtime included the unavoidable initial investment of time for ADE-related developments, which consumed about half of our total time, and an LCLS technical limitation during our experiments that only enabled us to trigger the pulses at 60 Hz or slower. Monitoring the presence of diffuse water scattering at 3.1 Å, we observed droplet hit ratios with the acoustic injectors of up to 88% in some data collection runs (Supplemental Information, and Figure S2A and Table S1). This enabled us to achieve a crystal hit ratio up to 50% for some samples, and an index ratio up to 30.4%. The modified Echo system produced a greater fraction of droplet hits, despite fewer crystal hits, in part because its ability to automatically adjust its acoustic pulse for different fluid types results in more reproducible droplet formation and trajectory. In one thermolysin data collection run the modified Echo system yielded over 20,000 droplet hits during an 8.5-min period at 60 Hz.

Unlike previous experiments requiring uniform crystal sizes for microjet injection, none of the samples were filtered prior to injection. The acoustic injector allowed us to launch different size crystals from our crystallization experiments, including several aliquots of Stc2 where crystals varied between 5 and 150 μm in diameter. Despite a 30-fold difference in sizes, Stc2 crystals produced diffraction in an average of 10% of X-ray pulses. Under ideal conditions both acoustic injectors were capable of launching crystal-containing droplets on demand at 500 Hz or more. However, during our beamtime the LCLS X-ray pulse triggering was disabled at 120 Hz for technical reasons at the facility; consequently, in order to time droplet delivery with the arrival of an X-ray pulse most of our runs were collected at 60 Hz or slower. Thermolysin, Stc2, and (less concentrated) lysozyme each diffracted beyond 1.9-Å resolution (Figure 2 and Tables S2– S4). As each sample was contained in a single well of a microplate, substantial sample throughput was also possible since sample change-over occurs in about a second.

Redox-Sensitive Samples Benefit from Combined SFX and Drop-On-Demand Methods

Redox-active proteins have evolved to facilitate electron exchange from one moiety to another, making their metal centers or organic cofactors sensitive to oxidation or reduction upon irradiation (Garman, 2010; Holton, 2009; Neutze et al., 2000; Sanishvili et al., 2011; Thurmer et al., 2013; Xu and Chance, 2007). Consequently, it can be difficult to compare structures of different redox forms of a protein obtained from synchrotron or home sources without concurrent spectroscopic monitoring of the reaction cycle during diffraction data collection (Daughtry et al., 2012). Unlike synchrotrons, FELs provide extremely powerful pulses lasting tens of femtoseconds or less. It is believed that the short FEL pulses terminate before primary and secondary photoelectric effects occur (Alonso-Mori et al., 2012; Nass et al., 2015; Neutze et al., 2000).

We studied four redox-active proteins at room temperature. PS-II contains a manganese cluster bound at its active site and represents a challenging case for SFX for two reasons. First, the multinuclear manganese complex is extremely sensitive to X-ray irradiation (Kern et al., 2013; Yano et al., 2005). Second, generating crystals small enough for microjet delivery can be incompatible with conditions needed to produce crystals that diffract to high resolution. This is particularly important for PS-II, but perhaps not as critical for many other systems that do produce microcrystal slurries and diffract well. Using the acoustic injector, crystals measuring 50–150 μm in diameter were delivered into the X-ray beam. Strong diffraction ($I/\sigma I > 2$) to better than 3.9 Å was observed for crystals grown in polyethylene glycol (PEG) 2000, corresponding to a ~0.5-Å improvement over previous SFX experiments on crystals obtained from similar preparations (Kern et al., 2013, 2014). In addition diffraction out to 2.8 Å for a novel PS-II crystal form in PEG 5000 (Hellmich et al., 2014) was obtained, representing the highest-resolution room temperature diffraction from PS-II observed so far.

Protein-bound iron centers that cycle through high valent states have been difficult to structurally characterize because of the transient nature of the intermediate species and susceptibility to reduction. One such system is the enzyme complex involving MauG (a c-type diheme enzyme) and its target protein MADH. MauG-MADH forms a high valence bis-Fe(IV) species through reaction with H_2O_2 that is kinetically stable but highly susceptible to reduction in the X-ray beam (Jensen et al., 2010; Wilmot and Yukl, 2013). For our tests, only 20–30 crystals were available, ranging in size from 10 to 50 μm along their longest edge. We observed settling of the crystals in their mother liquor within 1 min, making them ideal for the inverted system. Three diffraction patterns extending to 2.6 Å appeared within a minute of initiating injection (Figure 2).

We also tested three preparations of stachydrine demethylase (Stc2), a Rieske-type monooxygenase involved in converting strachydrine (*N,N*-dimethylproline) to *N*-methylproline and proline (Daughtry et al., 2012). Electrons generated through kGray X-ray irradiation are proposed to catalyze enzyme turnover, making it difficult to observe the enzyme-substrate complex. We prepared anaerobically purified, substrate-bound Stc2-stachydrine [ES] crystals as well as aerobically purified Stc2-stachydrine [E*S] and aerobically purified enzyme [E*] samples. Acoustically injected Stc2 crystals from these three batches yielded 26,365 crystal hits from which 13,002 were from the [ES] complex, 6,667 from the [E*S] complex, and 6,696 from the [E*] enzyme. Of those crystal hits 2,796 were indexed, integrated, and merged together to form one dataset (Table S2).

Although the microcrystal slurries for Stc2 were from three distinct types of samples, indexing the SFX runs from each type of sample confirmed that they were all isomorphous. Since there was insufficient data from each type of Stc2 to solve a structure on its own, we decided to merge the data from all the Stc2 runs (Figure 2). This yielded merging statistics and 3-Å resolution $F_o - F_c$ difference electron density maps from which the Rieske cluster was omitted (Figure 3) and a 2.2-Å partially refined structure (Table S2). The Rieske cluster, which was expected to be unchanged in all samples, exhibits well-resolved electron density. As anticipated, the electron density for the mononuclear iron site was ambiguous since some of the crystal slurry samples included substrate and others did not. Omit $F_o - F_c$ maps

confirmed the presence of the mononuclear iron and the three protein ligands, but the identity of exogenous ligands was not clear from the merged dataset.

The data collection and refinement statics, as well as an example of the electron density for a merged dataset of lysozyme, are presented in Table S3 and Figure S3. The statistics for a merged dataset of thermolysin are shown in Table S4. In all three cases the structures are not particularly well refined, which is consistent with the large *R* factor and *R*-free values. This is probably a result of relatively low redundancy of observed reflections, especially in the high-resolution shells.

Sample Considerations for Acoustic Injection

Maximizing droplet hit frequencies depends in part on reliably forming droplets with consistent trajectories. This requires optimization of the acoustic pulse structure, but is also affected by sample characteristics. Samples containing mainly salt-based reagents formed droplets with stable trajectories up to 14 mm away from the meniscus with both injectors. In contrast, solutions that are viscous or viscoelastic (wherein relaxation time is long relative to the other hydrodynamic timescales) typically yield less stable droplets because the hydrodynamics for these systems are not well behaved. Thus, samples containing polymers such as PEG exhibited delayed droplet pinch off compared with salts (see Supplemental Information and Table S1), but did form droplets readily at typical crystallization concentrations (0–30%, w/v). At the extreme, MauG-MADH samples in mother liquor containing 26% PEG 8,000 formed a fully connected liquid column up to 5–6-mm long from which droplets would pinch off from the column. Stc2 samples in about 10% or less PEG 3350 were more typical and ejected well without forming extended columns.

Similar to SFX experiments using microjets, the crystal hit frequency is proportional to the density of crystals in the sample. Acoustic injection of denser slurries, for example with a total crystal volume exceeding 75% of the sample volume, yielded crystal hits in up to 34% of recorded images. Samples with less than 10% relative crystal volume produced very infrequent crystal hits. With the modified Echo system and injecting upwards, we observed more frequent crystal hits in samples supplemented with agarose to keep them suspended. Most protein crystals are denser than their mother liquor, and tend to settle over time due to gravity. In our tests, the inverted system produced more frequent crystal hits from these samples. Crystal settling in the inverted configuration can be an advantage, since even samples with only a handful of crystals will concentrate at the meniscus. This was noted in the case of MauG-MADH, where relatively few droplets were injected before diffraction was observed. However, a disadvantage of the inverted system is that very dense crystal slurries can attenuate the acoustic energy and prevent droplet ejection.

Acoustic Injectors Complement Microjets

FELs with a photon energy in the hard X-ray regime (~9 keV) (Emma et al., 2010) make it possible to record diffraction from protein samples to atomic resolution (Schlichting, 2015). Most often, crystals are injected into the FEL beam in a continuous stream using either a gas dynamic virtual nozzle (GDVN), an electrospun liquid microjet (DePonte et al., 2008; Sierra et al., 2012; Weierstall, 2014), or a microextrusion injector for use with LCP (Caffrey et al.,

2014; Liu et al., 2013, 2014a, 2014b; Weierstall et al., 2014). Typically high-resolution diffraction data that are free of radiation-induced modifications are recorded from crystals roughly 100 nm up to 30 μm in diameter.

Acoustic injectors offer another method to deliver protein crystals into the pulsed FEL beam (Table 1). Microjets replenish microcrystals in the X-ray beam using a continuous stream of material, whereas each acoustic system delivers crystals in discrete droplets. To prevent clogging, continuous flow systems generally filter out crystals larger than 30 μm in diameter. The acoustic injectors do not clog, and can eject crystals larger than 400 μm. The greatest potential advantage of the acoustic injectors is their high crystal efficiency. In this study we were able to expose almost every other crystal to an X-ray pulse when conditions were optimized so that sufficient crystals are at the meniscus, but not so densely packed that they attenuated the acoustic energy. Consequently, about every other drop contained one or more crystals and over 80% of the drops were probed by the X-ray pulse. By comparison, continuous flow microjets typically expose one crystal for every 1,600 that pass through the interaction region during the time between X-ray pulses (Weierstall, 2014).

Diffraction from samples at ambient temperature and pressure at XPP typically produce Bragg reflections with lower mosaic spread than similar samples collected atcryogenic temperatures (Lovelace et al., 2006). Consequently, some of our samples gave diffraction where many of the peaks were recorded on single 110-μm square pixels of the CSPAD (see Supplemental Information and Figure S2B). An additional complication is the presence of multiple overlapping diffraction patterns when more than one crystal is in a single droplet. Deconvolution of more than one lattice is challenging for current data-processing programs designed for handling diffraction data from FELs (Sauter, 2015; Sauter and Poon, 2010).

DISCUSSION

Two acoustic injectors were deployed at the XPP instrument of the LCLS with the goal of demonstrating drop-on-demand sample delivery into the pulsed X-ray beam. Acoustic injectors efficiently use crystals with dimensions greater than 5 μm and are compatible with most standard crystallization conditions. Furthermore, the method is gentle on the crystal lattice (Soares et al., 2011; Villaseñor et al., 2010; Yin et al., 2014). The modified Echo system offers high automation and speed, along with repeatable droplet volumes and velocities. The inverted system features selectable droplet sizes and an upside-down configuration to counteract crystal settling. Both acoustic injectors can change from one sample to another by ejecting from wells within standard crystallization plates, and with minimal impact on experiment time.

Future applications of acoustic-based, drop-on-demand, serial crystallography are envisioned for synchrotron and XFEL sources. An acoustic injector can deposit samples onto a conveyor belt system, which translates crystal-containing droplets into a synchrotron X-ray beam (Heroux et al., 2014; Roessler et al., 2013). We are extending this concept to ongoing XFEL experiments in support of time-resolved SFX with complementary X-ray spectroscopic measurements.

We used different transducer frequencies in our acoustic injectors to produce droplets with diameters that ranged from ~50 to 200 μm. This is considerably larger than jets that can produce streams of only ~5 μm diameter. Because acoustic injectors place more solvent in the X-ray beam, they also yield more background scattering. Consequently, acoustic injectors are best suited to slurries made up of larger microcrystals that yield stronger diffraction patterns. Indeed, we anticipate that submicrometer-sized crystals are not well matched for acoustic injectors since the weaker diffraction patterns are likely to be swamped by background scatter from the droplet.

An advantage of the acoustic injector is that it only delivers a sample to the interaction region when an X-ray pulse is present. Since every 50-fs pulse is followed by over 8.3 ms of dark time at the LCLS, this alone potentiates many orders of magnitude increase in efficiency as no sample is consumed during the dark period. Continued refinement of our methods will ensure that each droplet is probed by X-rays and that it contains one crystal on average. Meeting these goals will reduce the time needed to collect a complete high-resolution dataset to just a few minutes at the LCLS.

We note that our acoustic methods have potential for applications at synchrotron X-ray sources. For example, the Frontier Macromolecular Crystallography (FMX) beamline at NSLS-II anticipates delivering ~10^{13} photons s^{-1} at 1-Å wavelength in a 1-μm^2 focused X-ray beam, and the MicroMax beamline at Max-IV may be 100-fold brighter in polychromatic (pink beam) mode. We have shown that a ~10-kGy dose yields high-resolution diffraction patterns and very often spectroscopic changes to, for example, the heme moiety from myoglobin crystals (Yi et al., 2010) or the bilin chromophore within phytochrome crystals (Li et al., 2015). Using RADDOSE (Paithankar and Garman, 2010) we estimate that a 10-kGy dose can be delivered to a 1-μm^3 myoglobin microcrystal at FMX in about 1 μs. This is the same time required for such a crystal within an ADE-launched droplet traveling at 1 m s^{-1} to traverse the focused FMX X-ray beam. Larger crystals will take proportionally longer to pass through small X-ray beams, but from which only 1 μm^2 is exposed for each microsecond. Similarly, larger X-ray beams can expose larger crystals for longer times. Eventually the room temperature dose limit will be reached (estimated without regard to dose rate at about 100-fold less than 20 MGy cryogenic limit, or approximately 200 kGy), which could be as quick as 20 μs at FMX with a stationary crystal. Of course this will be even faster with pink beam and, thus, it is possible that an acoustically launched 20-μm^3 crystal could be taken to nearly the dose limit as it traverses the X-ray beam.

EXPERIMENTAL PROCEDURES

Cloning, expression, purification, and/or crystallization of the proteins are detailed in Supplemental Information and references therein. Briefly, thermolysin, HEWL, and PS-II were crystallized using a batch method. HEWL (70 mg/ml) in 20 mM Na acetate (pH 4.6) was mixed with precipitant (20 mM Na acetate [pH 4.6], 8%, w/v, NaCl, 10%, v/v, ethylene glycol). Thermolysin (30 mg/ml) in 50 mM NaOH was mixed with 15% (w/v) ammonium sulfate. PS-II (40 mg/ml in 100 mM piperazine-*N,N*′-bis(ethanesulfonic acid) [PIPES; pH 7.0], 5 mM $CaCl_2$, 0.03% β-dodecyl maltoside) was mixed with 8% (w/v) PEG 2000 in 100 mM PIPES (pH 7.0), 5 mM $CaCl_2$ and were harvested with 10% (w/v) PEG 2000 in 100

mM PIPES (pH 7.0), 5 mM $CaCl_2$. Alternatively, PS-II (20 mg/ml in 0.02 M 2-(*N*-morpholino)ethanesulfonic acid [MES; pH 6.0], 0.01 M $CaCl_2$, and 0.013% $C_{12}E_8$) in octaethyleneglycolmonododecylether ($C_{12}E_8$) detergent was mixed with the precipitant (0.1 M Tris [pH 7.5], 0.1 M $(NH_4)_2SO_4$, 15%–18% PEG 5000 mono methylether [MME]), harvested with 0.1 M Tris (pH 7.5), 0.1 M $(NH_4)_2SO_4$, 10% PEG 5000 MME, and then stepwise transferred into the same buffer containing 40% PEG 5000 MME.

Crystals of extracellular hemoglobin from *G. paulistus* (oxy-HbGp), diferrous Fe(II)-MauG-MADH, and Stc2 were grown by hanging drop vapor diffusion. Oxy-HbGp (18 mg/ml in 100 mM Tris-HCl [pH 7.5]) was mixed with precipitant (1.6 M K_2HPO_4 [pH 9.0]) and equilibrated at room temperature. For the MauG-MADH complex, the protein sample contained 100 μM MauG, 50 μM MADH, and 2 mM Na dithionite in 10 mM potassium phosphate (pH 7.5) over a reservoir of 22%–26% (w/v) PEG 8000, 100 mM Na acetate, 100 mM MES [pH 6.4]). Just prior to data collection, H_2O_2 in crystal mother liquor was added to a final concentration of 2 mM to generate the bis-Fe(IV) state of the MauG in the MauG-MADH crystals. Stc2 (35 mg/ml in 10 mM Tris buffer [pH 7.5], 2.5 mM biotin) was crystallized over a reservoir containing 15% PEG 3350, 20% glycerol, 100 mM succinic acid (pH 7.0), and 10 mM hexamine cobalt.

Acoustic Injector Designs

The two acoustic injectors are described more fully in Supplemental Information. Briefly, in the modified Echo 555 the acoustic transducer assembly and water bubbling column were placed external to the systems controls. The inverted injector is based on an acoustic reagent multispotter (Aerni et al., 2005). This device consists of an arbitrary waveform generator (Tabor Electronics), a 150-W broadband radiofrequency (rf) amplifier (Amplifier Research), and several spot-focused piezoelectric transducers (Olympus NDT) with center frequencies at 10, 15, and 25 MHz. Each transducer was excited at its peak frequency by a sine wave pulse of 60–400 μs duration. Signal amplitude was controlled through the waveform generator and the rf amplifier, and was varied along with the sine pulse duration to produce 20 mW root mean square per burst. Acoustic coupling was accomplished using either a 20-mm (for the 10- and 15-MHz transducers) or a 6-mm tall column of boiled and cooled 0.5% (w/v) agarose. Control of the modified Echo 555 and the inverted injector was accomplished by providing a transistor-transistor logic trigger signal from the LCLS to the respective software controllers. During the experiment the waveform characteristics were monitored with a digital oscilloscope using an inline 30-dB dual directional coupler (Werlatone) placed between the amplifier and the transducer.

Supplementary Material

Refer to Web version on PubMed Central for supplementary material.

Acknowledgments

Experiments were carried out at the LCLS, a national user facility operated by Stanford University on behalf of the US Department of Energy (DOE), Office of Basic Energy Sciences (OBES). Use of the Linac Coherent Light Source (LCLS), SLAC National Accelerator Laboratory, is supported by the U.S. Department of Energy, Office of Science, Office of Basic Energy Sciences under Contract No. DE-AC02-76SF00515. We thank the staff at LCLS/

SLAC for their support. This work was supported by the Brookhaven National Laboratory/US DOE, Laboratory Directed Research and Development grant 11-008 (A.S.S., M.A., and A.M.O.); NIH/NCRR grant 2-P41-RR012408, NIH/National Institute of General Medical Sciences (NIGMS) grant 8P41GM103473-16 and the US DOE, Office of Biological and Environmental Research (OBER) grant FWP BO-70 (A.H., A.M.O., and A.S.S); NIH NIGMS grant Y1GM008003 (M.A.); and the Brookhaven National Laboratory Biosciences Department grant BO-9734 (R.A.). NIH grants GM095887 and GM102520 and Director, Office of Science, DOE under contract DE-AC02-05CH11231 for data-processing methods (A.S.B. and N.K.S.). NIH 5R01 GM066569-11 (C.M.W.), NIH 5R37 GM041574-26 (V.L.D.), NIH F32 GM097779-03 (E.T.Y.) for MauG-MADH biochemistry. Anaerobically purified Stc2 production was supported by the National Science Foundation grant CHE 0748504 (P.L.). PS-II production and crystallization was supported by the US DOE Director, Office of Science, OBES, Division of Chemical Sciences, Geosciences, and Biosciences (CSGB) under contract DE-AC02-05CH11231 (J.Y. and V.K.Y.); NIH grants GM055302 (V.K.Y.) and GM110501 (J.Y.), the Human Frontiers Science Project (J.Y. and A.Z.), the DFG-Cluster of Excellence “UniCat” coordinated by the Technische Universität Berlin and Sfb1078, TP A5 (A.Z.). Testing of crystals and various parts of the setup were carried out at synchrotron facilities that were provided by the Advanced Light Source (ALS) in Berkeley, the National Synchrotron Light Source (NSLS) in Upton, NY, and the Stanford Synchrotron Radiation Lightsource (SSRL). Use of the National Synchrotron Light Source, Brookhaven National Laboratory, was supported by the US Department of Energy, Office of Science, Office of Basic Energy Sciences, under contract no. DE-AC02-98CH10886. Use of the Stanford Synchrotron Radiation Light-source, SLAC National Accelerator Laboratory, is supported by the US Department of Energy, Office of Science, Office of Basic Energy Sciences under contract no. DE-AC02-76SF00515. The SSRL Structural Molecular Biology Program is supported by the DOE Office of Biological and Environmental Research, and by the NIH, National Institute of General Medical Sciences (including P41GM103393). Richard Ellson is a founder and a member of the Board of Directors of Labcyte Inc. S.D., B.E., L.P.G., L.M., W.M.M., J.O., and R.G.S. are employed by Labcyte Inc.

REFERENCES

Aerni H-R, Cornett DS, Caprioli RM. Automated acoustic matrix deposition for MALDI sample preparation. Anal. Chem. 2005; 78:827–834. [PubMed: 16448057]

Alonso-Mori R, Kern J, Gildea RJ, Sokaras D, Weng TC, Lassalle-Kaiser B, Tran R, Hattne J, Laksmono H, Hellmich J, et al. Energy-dispersive X-ray emission spectroscopy using an X-ray free-electron laser in a shot-by-shot mode. Proc. Natl. Acad. Sci. USA. 2012; 109:19103–19107. [PubMed: 23129631]

Aquila A, Hunter MS, Doak RB, Kirian RA, Fromme P, White TA, Andreasson J, Arnlund D, Bajt S, Barends TR, et al. Time-resolved protein nanocrystallography using an X-ray free-electron laser. Opt. Express. 2012; 20:2706–2716. [PubMed: 22330507]

Bachega JF, Bleicher L, Horjales ER, Santiago PS, Garratt RC, Tabak M. Crystallization and preliminary structural analysis of the giant haemoglobin from *Glossoscolex paulistus* at 3.2 A. J. Synchrotron Radiat. 2011; 18:24–28. [PubMed: 21169685]

Barends TRM, Foucar L, Botha S, Doak RB, Shoeman RL, Nass K, Koglin JE, Williams GJ, Boutet S, Messerschmidt M, et al. De novo protein crystal structure determination from X-ray free-electron laser data. Nature. 2014; 505:244–247. [PubMed: 24270807]

Boutet S, Lomb L, Williams GJ, Barends TR, Aquila A, Doak RB, Weierstall U, DePonte DP, Steinbrener J, Shoeman RL, et al. High-resolution protein structure determination by serial femtosecond crystallography. Science. 2012; 337:362–364. [PubMed: 22653729]

Caffrey M, Li D, Howe N, Shah ST. ‘Hit and run’ serial femtosecond crystallography of a membrane kinase in the lipid cubic phase. Philos. Trans. R. Soc. Lond. B Biol. Sci. 2014; 369:20130621. [PubMed: 24914170]

Chapman HN, Fromme P, Barty A, White TA, Kirian RA, Aquila A, Hunter MS, Schulz J, DePonte DP, Weierstall U, et al. Femtosecond X-ray protein nanocrystallography. Nature. 2011; 470:73–77. [PubMed: 21293373]

Chapman HN, Caleman C, Timneanu N. Diffraction before destruction. Philos. Trans. R. Soc. Lond. B Biol. Sci. 2014; 369:20130313. [PubMed: 24914146]

Chollet M, Alonso-Mori R, Cammarata M, Damiani D, Defever J, Delor JT, Feng Y, Glownia JM, Langton JB, Nelson S, et al. The X-ray pump-probe instrument at the linac coherent light source. J. Synchrotron Radiat. 2015; 22:503–507. [PubMed: 25931060]

Cohen AE, Soltis SM, Gonzalez A, Aguila L, Alonso-Mori R, Barnes CO, Baxter EL, Brehmer W, Brewster AS, Brunger AT, et al. Goniometer-based femtosecond crystallography with X-ray free electron lasers. Proc. Natl. Acad. Sci. USA. 2014; 111:17122–17127. [PubMed: 25362050]

Cole K, Roessler CG, Mule EA, Benson-Xu EJ, Mullen JD, Le BA, Tieman AM, Birone C, Brown M, Hernandez J, et al. A linear relationship between crystal size and fragment binding time observed crystallo-graphically: implications for fragment library screening using acoustic droplet ejection. PLoS One. 2014; 9:e101036. [PubMed: 24988328]

Conrad CE, Basu S, James D, Wang D, Schaffer A, Roy-Chowdhury S, Zatsepin NA, Aquila A, Coe J, Gati C, et al. A novel inert crystal delivery medium for serial femtosecond crystallography. IUCrJ. 2015; 2:421–430.

Coquelle N, Brewster AS, Kapp U, Shilova A, Weinhausen B, Burghammer M, Colletier JP. Raster-scanning serial protein crystallography using micro- and nano-focused synchrotron beams. Acta Crystallogr. D Biol. Crystallogr. 2015; 71:1184–1196. [PubMed: 25945583]

Cuttitta CM, Ericson DL, Scalia A, Roessler CG, Teplitsky E, Joshi K, Campos O, Agarwal R, Allaire M, Orville AM, et al. Acoustic transfer of protein crystals from agarose pedestals to micromeshes for high-throughput screening. Acta Crystallogr. D Biol. Crystallogr. 2015; 71:94–103. [PubMed: 25615864]

Daughtry KD, Xiao Y, Stoner-Ma D, Cho E, Orville AM, Liu P, Allen KN. Quaternary ammonium oxidative demethylation: X-ray crystallographic, resonance Raman, and UV-visible spectroscopic analysis of a Rieske-type demethylase. J. Am. Chem. Soc. 2012; 134:2823–2834. [PubMed: 22224443]

Demirci H, Sierra RG, Laksmono H, Shoeman RL, Botha S, Barends TRM, Nass K, Schlichting I, Doak RB, Gati C, et al. Serial femtosecond X-ray diffraction of 30S ribosomal subunit microcrystals in liquid suspension at ambient temperature using an X-ray free-electron laser. Acta Crystallogr. Sect F Struct. Biol. Cryst. Commun. 2013; 69:1066–1069.

DePonte DP, Weierstall U, Schmidt K, Warner J, Starodub D, Spence JCH, Doak RB. Gas dynamic virtual nozzle for generation of microscopic droplet streams. J. Phys. D Appl. Phys. 2008; 41:195505.

Ellson R, Mutz M, Browning B, Lee L, Miller MF, Papen R. Transfer of low nanoliter volumes between microwell plates using focused acoustics - automation considerations. J. Assoc. Lab. Autom. 2003; 8:29–34.

Emma P, Akre R, Arthur J, Bionta R, Bostedt C, Bozek J, Brachmann A, Bucksbaum P, Coffee R, Decker FJ, et al. First lasing and operation of an angstrom-wavelength free-electron laser. Nat. Photon. 2010; 4:641–647.

Garman EF. Radiation damage in macromolecular crystallography: what is it and why should we care? Acta Crystallogr. D Biol. Crystallogr. 2010; 66:339–351. [PubMed: 20382986]

Hart P, Boutet S, Carini G, Dubrovin M, Duda B, Fritz D, Haller G, Herbst R, Herrmann S, Kenney C, et al. The CSPAD megapixel x-ray camera at LCLS. Proc. SPIE. 2012; 8504:85040C.

Hattne J, Echols N, Tran R, Kern J, Gildea RJ, Brewster AS, Alonso-Mori R, Glockner C, Hellmich J, Laksmono H, et al. Accurate macromolecular structures using minimal measurements from X-ray free-electron lasers. Nat. Methods. 2014; 11:545–548. [PubMed: 24633409]

Hellmich J, Bommer M, Burkhardt A, Ibrahim M, Kern J, Meents A, Muh F, Dobbek H, Zouni A. Native-like photosystem II superstructure at 2.44 A resolution through detergent extraction from the protein crystal. Structure. 2014; 22:1607–1615. [PubMed: 25438669]

Heroux A, Allaire M, Buono R, Cowan ML, Dvorak J, Flaks L, Lamarra S, Myers SF, Orville AM, Robinson HH, et al. Macromolecular crystallography beamline X25 at the NSLS. J. Synchrotron Radiat. 2014; 21:627–632. [PubMed: 24763654]

Hirata K, Shinzawa-Itoh K, Yano N, Takemura S, Kato K, Hatanaka M, Muramoto K, Kawahara T, Tsukihara T, Yamashita E, et al. Determination of damage-free crystal structure of an X-ray-sensitive protein using an XFEL. Nat. Methods. 2014; 11:734–736. [PubMed: 24813624]

Holton JM. A beginner's guide to radiation damage. J. Synchrotron Radiat. 2009; 16:133–142. [PubMed: 19240325]

Hunter MS, Segelke B, Messerschmidt M, Williams GJ, Zatsepin NA, Barty A, Benner WH, Carlson DB, Coleman M, Graf A, et al. Fixed-target protein serial microcrystallography with an x-ray free electron laser. Sci. Rep. 2014; 4:6026. [PubMed: 25113598]

Jensen LM, Sanishvili R, Davidson VL, Wilmot CM. In crystallo posttranslational modification within a MauG/pre-methylamine dehydrogenase complex. Science. 2010; 327:1392–1394. [PubMed: 20223990]

Johansson LC, Arnlund D, White TA, Katona G, Deponte DP, Weierstall U, Doak RB, Shoeman RL, Lomb L, Malmerberg E, et al. Lipidic phase membrane protein serial femtosecond crystallography. Nat. Methods. 2012; 9:263–265. [PubMed: 22286383]

Johansson LC, Arnlund D, Katona G, White TA, Barty A, DePonte DP, Shoeman RL, Wickstrand C, Sharma A, Williams GJ, et al. Structure of a photosynthetic reaction centre determined by serial femtosecond crystallography. Nat. Commun. 2013; 4:2911. [PubMed: 24352554]

Kang Y, Zhou XE, Gao X, He Y, Liu W, Ishchenko A, Barty A, White TA, Yefanov O, Han GW, et al. Crystal structure of rhodopsin bound to arrestin by femtosecond X-ray laser. Nature. 2015; 523:561–567. [PubMed: 26200343]

Kern J, Loll B, Lüneberg C, DiFiore D, Biesiadka J, Irrgang KD, Zouni A. Purification, characterisation and crystallisation of photosystem II from *Thermosynechococcus elongatus* cultivated in a new type of photobioreactor. Biochim. Biophys. Acta. 2005; 1706:147–157. [PubMed: 15620375]

Kern J, Alonso-Mori R, Hellmich J, Tran R, Hattne J, Laksmono H, Glockner C, Echols N, Sierra RG, Sellberg J, et al. Room temperature femtosecond X-ray diffraction of photosystem II microcrystals. Proc. Natl. Acad. Sci. USA. 2012; 109:9721–9726. [PubMed: 22665786]

Kern J, Alonso-Mori R, Tran R, Hattne J, Gildea RJ, Echols N, Glockner C, Hellmich J, Laksmono H, Sierra RG, et al. Simultaneous femtosecond X-ray spectroscopy and diffraction of photosystem II at room temperature. Science. 2013; 340:491–495. [PubMed: 23413188]

Kern J, Tran R, Alonso-Mori R, Koroidov S, Echols N, Hattne J, Ibrahim M, Gul S, Laksmono H, Sierra RG, et al. Taking snapshots of photosynthetic water oxidation using femtosecond X-ray diffraction and spectroscopy. Nat. Commun. 2014; 5:4371. [PubMed: 25006873]

Li F, Burgie ES, Yu T, Heroux A, Schatz GC, Vierstra RD, Orville AM. X-ray radiation induces deprotonation of the bilin chromophore in crystalline *D. radiodurans* phytochrome. J. Am. Chem. Soc. 2015; 137:2792–2795. [PubMed: 25650486]

Liu W, Wacker D, Gati C, Han GW, James D, Wang D, Nelson G, Weierstall U, Katritch V, Barty A, et al. Serial femtosecond crystallography of G protein-coupled receptors. Science. 2013; 342:1521–1524. [PubMed: 24357322]

Liu W, Ishchenko A, Cherezov V. Preparation of microcrystals in lipidic cubic phase for serial femtosecond crystallography. Nat. Protoc. 2014a; 9:2123–2134. [PubMed: 25122522]

Liu W, Wacker D, Wang C, Abola E, Cherezov V. Femtosecond crystallography of membrane proteins in the lipidic cubic phase. Philos. Trans. R. Soc. Lond. B Biol. Sci. 2014b; 369:20130314. [PubMed: 24914147]

Lomb L, Barends TRM, Kassemeyer S, Aquila A, Epp SW, Erk B, Foucar L, Hartmann R, Rudek B, Rolles D, et al. Radiation damage in protein serial femtosecond crystallography using an X-ray free-electron laser. Phys. Rev. B Condens. Matter Mater. Phys. 2011; 84:214111. [PubMed: 24089594]

Lovelace JJ, Murphy CR, Pahl R, Brister K, Borgstahl GEO. Tracking reflections through cryogenic cooling with topography. J. Appl. Crystallogr. 2006; 39:425–432.

Moeller S, Arthur J, Brachmann A, Coffee R, Decker FJ, Ding Y, Dowell D, Edstrom S, Emma P, Feng Y, et al. Photon beamlines and diagnostics at LCLS. Nucl. Instrum. Methods Phys. Res. A. 2011; 635:S6–S11.

Mueller C, Marx A, Epp SW, Zhong Y, Kuo A, Balo AR, Soman J, Schotte F, Lemke HT, Owen RL, et al. Fixed target matrix for femtosecond time-resolved and in situ serial microcrystallography. Struct. Dyn. 2015; 2:054302. [PubMed: 26798825]

Nass K, Foucar L, Barends TR, Hartmann E, Botha S, Shoeman RL, Doak RB, Alonso-Mori R, Aquila A, Bajt S, et al. Indications of radiation damage in ferredoxin microcrystals using high-intensity X-FEL beams. J. Synchrotron Radiat. 2015; 22:225–238. [PubMed: 25723924]

Neutze R, Wouts R, van der Spoel D, Weckert E, Hajdu J. Potential for biomolecular imaging with femtosecond X-ray pulses. Nature. 2000; 406:752–757. [PubMed: 10963603]

Paithankar KS, Garman EF. Know your dose: RADDOSE. Acta Crystallogr. D Biol. Crystallogr. 2010; 66:381–388. [PubMed: 20382991]

Redecke L, Nass K, DePonte DP, White TA, Rehders D, Barty A, Stellato F, Liang M, Barends TR, Boutet S, et al. Natively inhibited *Trypanosoma brucei* cathepsin B structure determined by using an X-ray laser. Science. 2013; 339:227–230. [PubMed: 23196907]

Roedig P, Vartiainen I, Duman R, Panneerselvam S, Stube N, Lorbeer O, Warmer M, Sutton G, Stuart DI, Weckert E, et al. A micro-patterned silicon chip as sample holder for macromolecular crystallography experiments with minimal background scattering. Sci. Rep. 2015; 5:10451. [PubMed: 26022615]

Roessler CG, Kuczewski A, Stearns R, Ellson R, Olechno J, Orville AM, Allaire M, Soares AS, Heroux A. Acoustic methods for high-throughput protein crystal mounting at next-generation macromolecular crystallographic beamlines. J. Synchrotron Radiat. 2013; 20:805–808. [PubMed: 23955046]

Ruggiero Bachega JF, Vasconcelos Maluf F, Andi B, D'Muniz Pereira H, Falsarella Carazzollea M, Orville AM, Tabak M, Brandao-Neto J, Garratt RC, Horjales Reboredo E. The structure of the giant haemoglobin from *Glossoscolex paulistus* . Acta Crystallogr. D Biol. Crystallogr. 2015; 71:1257–1271. [PubMed: 26057666]

Sanishvili R, Yoder DW, Pothineni SB, Rosenbaum G, Xu S, Vogt S, Stepanov S, Makarov OA, Corcoran S, Benn R, et al. Radiation damage in protein crystals is reduced with a micron-sized X-ray beam. Proc. Natl. Acad. Sci. USA. 2011; 108:6127–6132. [PubMed: 21444772]

Sauter NK. XFEL diffraction: developing processing methods to optimize data quality. J. Synchrotron Radiat. 2015; 22:239–248. [PubMed: 25723925]

Sauter NK, Poon BK. Autoindexing with outlier rejection and identification of superimposed lattices. J. Appl. Crystallogr. 2010; 43:611–616. [PubMed: 20502598]

Schlichting I. Serial femtosecond crystallography: the first five years. IUCrJ. 2015; 2:246–255.

Sierra RG, Laksmono H, Kern J, Tran R, Hattne J, Alonso-Mori R, Lassalle-Kaiser B, Glockner C, Hellmich J, Schafer DW, et al. Nanoflow electrospinning serial femtosecond crystallography. Acta Crystallogr. D Biol. Crystallogr. 2012; 68:1584–1587. [PubMed: 23090408]

Soares AS, Engel MA, Stearns R, Datwani S, Olechno J, Ellson R, Skinner JM, Allaire M, Orville AM. Acoustically mounted micro-crystals yield high-resolution X-ray structures. Biochemistry. 2011; 50:4399–4401. [PubMed: 21542590]

Suga M, Akita F, Hirata K, Ueno G, Murakami H, Nakajima Y, Shimizu T, Yamashita K, Yamamoto M, Ago H, et al. Native structure of photosystem II at 1.95 A resolution viewed by femtosecond X-ray pulses. Nature. 2015; 517:99–103. [PubMed: 25470056]

Sugahara M, Mizohata E, Nango E, Suzuki M, Tanaka T, Masuda T, Tanaka R, Shimamura T, Tanaka Y, Suno C, et al. Grease matrix as a versatile carrier of proteins for serial crystallography. Nat. Methods. 2015; 12:61–63. [PubMed: 25384243]

Teplitsky E, Joshi K, Ericson DL, Scalia A, Mullen JD, Sweet RM, Soares AS. High throughput screening using acoustic droplet ejection to combine protein crystals and chemical libraries on crystallization plates at high density. J. Struct. Biol. 2015; 191:49–58. [PubMed: 26027487]

Thurmer S, Oncak M, Ottosson N, Seidel R, Hergenhahn U, Bradforth SE, Slavicek P, Winter B. On the nature and origin of dicationic, charge-separated species formed in liquid water on X-ray irradiation. Nat. Chem. 2013; 5:590–596. [PubMed: 23787749]

Villaseñor AG, Wong A, Shao A, Garg A, Kuglstatter A, Harris SF. Acoustic matrix microseeding: improving protein crystal growth with minimal chemical bias. Acta Crystallogr. D Biol. Crystallogr. 2010; 66:568–576. [PubMed: 20445232]

Villaseñor AG, Wong A, Shao A, Garg A, Donohue TJ, Kuglstatter A, Harris SF. Nanolitre-scale crystallization using acoustic liquid-transfer technology. Acta Crystallogr. D Biol. Crystallogr. 2012; 68:893–900. [PubMed: 22868754]

Weierstall U. Liquid sample delivery techniques for serial femtosecond crystallography. Philos. Trans. R. Soc. Lond. B Biol. Sci. 2014; 369:20130337. [PubMed: 24914163]

Weierstall U, James D, Wang C, White TA, Wang D, Liu W, Spence JC, Bruce Doak R, Nelson G, Fromme P, et al. Lipidic cubic phase injector facilitates membrane protein serial femtosecond crystallography. Nat. Commun. 2014; 5:3309. [PubMed: 24525480]

Wilmot CM, Yukl ET. MauG: a di-heme enzyme required for methylamine dehydrogenase maturation. Dalton Trans. 2013; 42:3127–3135. [PubMed: 23086017]

Xu G, Chance MR. Hydroxyl radical-mediated modification of proteins as probes for structural proteomicsv. Chem. Rev. 2007; 107:3514–3543. [PubMed: 17683160]

Yano J, Kern J, Irrgang KD, Latimer MJ, Bergmann U, Glatzel P, Pushkar Y, Biesiadka J, Loll B, Sauer K, et al. X-ray damage to the Mn_4Ca complex in single crystals of photosystem II: a case study for metal-loprotein crystallography. Proc. Natl. Acad. Sci. USA. 2005; 102:12047–12052. [PubMed: 16103362]

Yi J, Orville AM, Skinner JM, Skinner MJ, Richter-Addo GB. Synchrotron X-ray-induced photoreduction of ferric myoglobin nitrite crystals gives the ferrous derivative with retention of the O-bonded nitrite ligand. Biochemistry. 2010; 49:5969–5971. [PubMed: 20568729]

Yin X, Scalia A, Leroy L, Cuttitta CM, Polizzo GM, Ericson DL, Roessler CG, Campos O, Ma MY, Agarwal R, et al. Hitting the target: fragment screening with acoustic in situ co-crystallization of proteins plus fragment libraries on pin-mounted data-collection micromeshes. Acta Crystallogr. D Biol. Crystallogr. 2014; 70:1177–1189. [PubMed: 24816088]

Yukl ET, Jensen LM, Davidson VL, Wilmot CM. Structures of MauG in complex with quinol and quinone MADH. Acta Crystallogr. Sect F Struct. Biol. Cryst. Commun. 2013; 69:738–743.

Highlights

- Acoustic methods inject crystal-containing droplets directly from microplate wells
- On-demand acoustic injection uses crystals efficiently without orifices or clogging
- Diffraction patterns from crystals measuring several tens of μm are of high quality
- Complete datasets can be obtained from fewer than 50,000 crystals

In Brief

Acoustic droplet ejection provides an automated tool for efficient use of protein crystals in SFX experiments. Roessler et al. used this method to deliver crystal-containing droplets into the XFEL beam to coincide with each X-ray pulse.

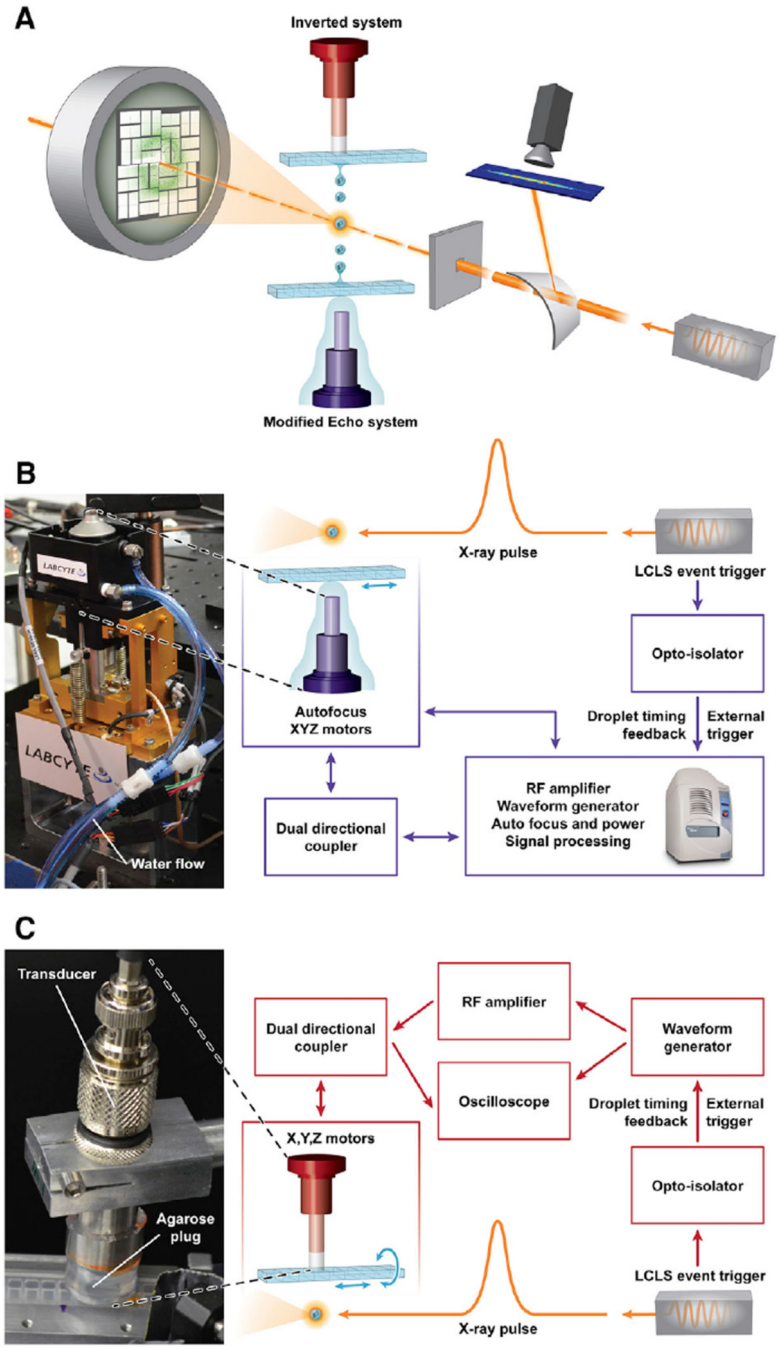

Figure 1. Acoustic Injection for SFC

(A) Schematic overview image shows incoming X-ray pulses passing first through a bent transmissive silicon crystal, deflecting a portion of each pulse for spectrographic recording. The pulses arrive at the interaction region concurrent with a crystal-containing droplet. In the inverted system, the droplet is ejected downward out of a multiwell microplate. The modified Echo system is configured to eject droplets upwards out of a multiwell microplate. Diffraction patterns were recorded 108 mm downstream of the interaction point by a

Cornell-SLAC pixel array detector. The three drops are meant to illustrate the repeatable nature of the ejection process and are not to scale.

(B) Detail for the modified Echo system in which the acoustic injector (photo, left) was controlled through an “umbilical cord” with electrical and water connections to the Echo instrument.

(C) Detail for the inverted system wherein an agarose plug maintained the acoustic connection between the transducer and the inverted microplate well (photo, left). Illustration courtesy Tiffany Bowman, BNL. See also Figure S1.

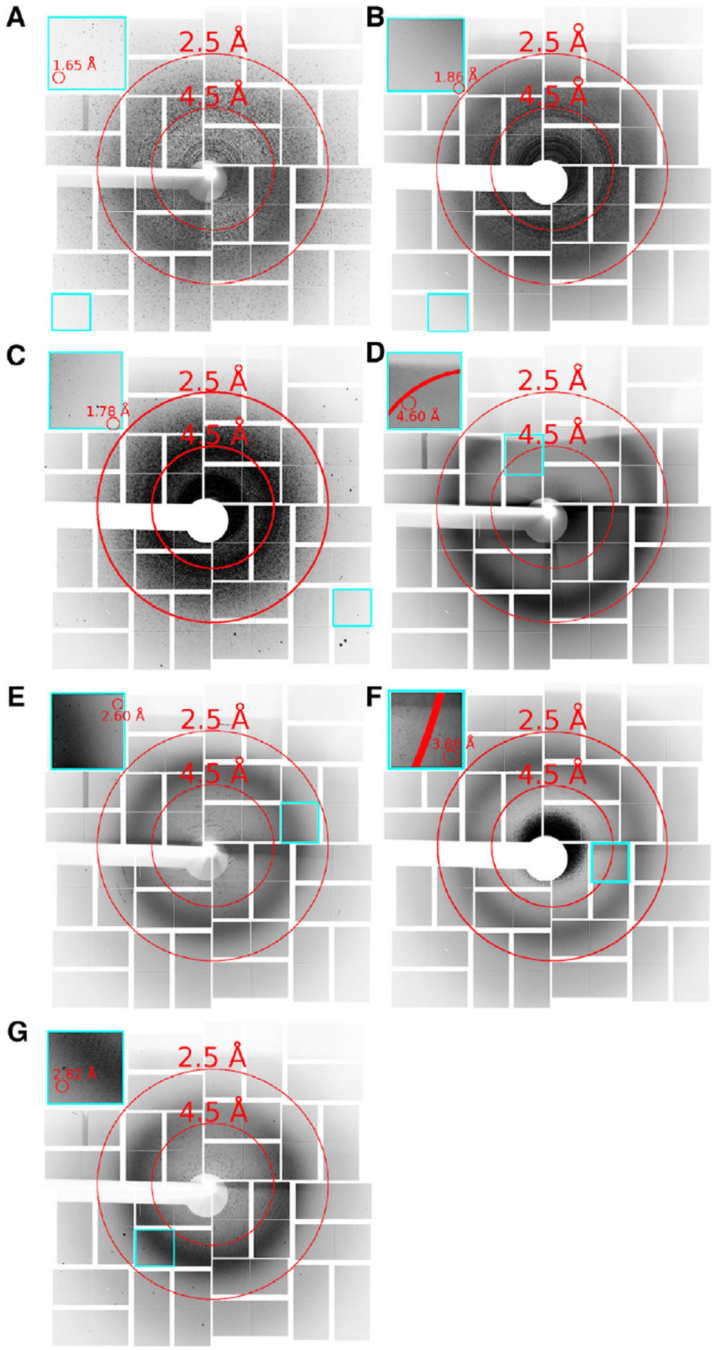

Figure 2. An Overlay, Composite, or Virtual Powder Pattern of the Diffraction Hits Observed for Acoustically Injected Samples

(A–G) Images show the maximum pixel values over selected runs merged by sample type. (A) Lysozyme (7,613 images), (B) Thermolysin (18,172 images), (C) Stc2 (26,365 images), (D) giant extracellular hemoglobin (554 images), (E) MauG-MADH (17,217 images), (F) PS-II in PEG 2000 (42,046 images), and (G) PS-II in PEG 5000 (18,197 images). Insets highlighted in cyan show individual application-specific integrated circuit tiles containing the highest-resolution reflections for each sample. Shadows appear on the top of the detector

in some cases from positioning the sample holder within the cone of X-ray scatter. Some diffraction images contained multiple patterns per image. See also Figure S2.

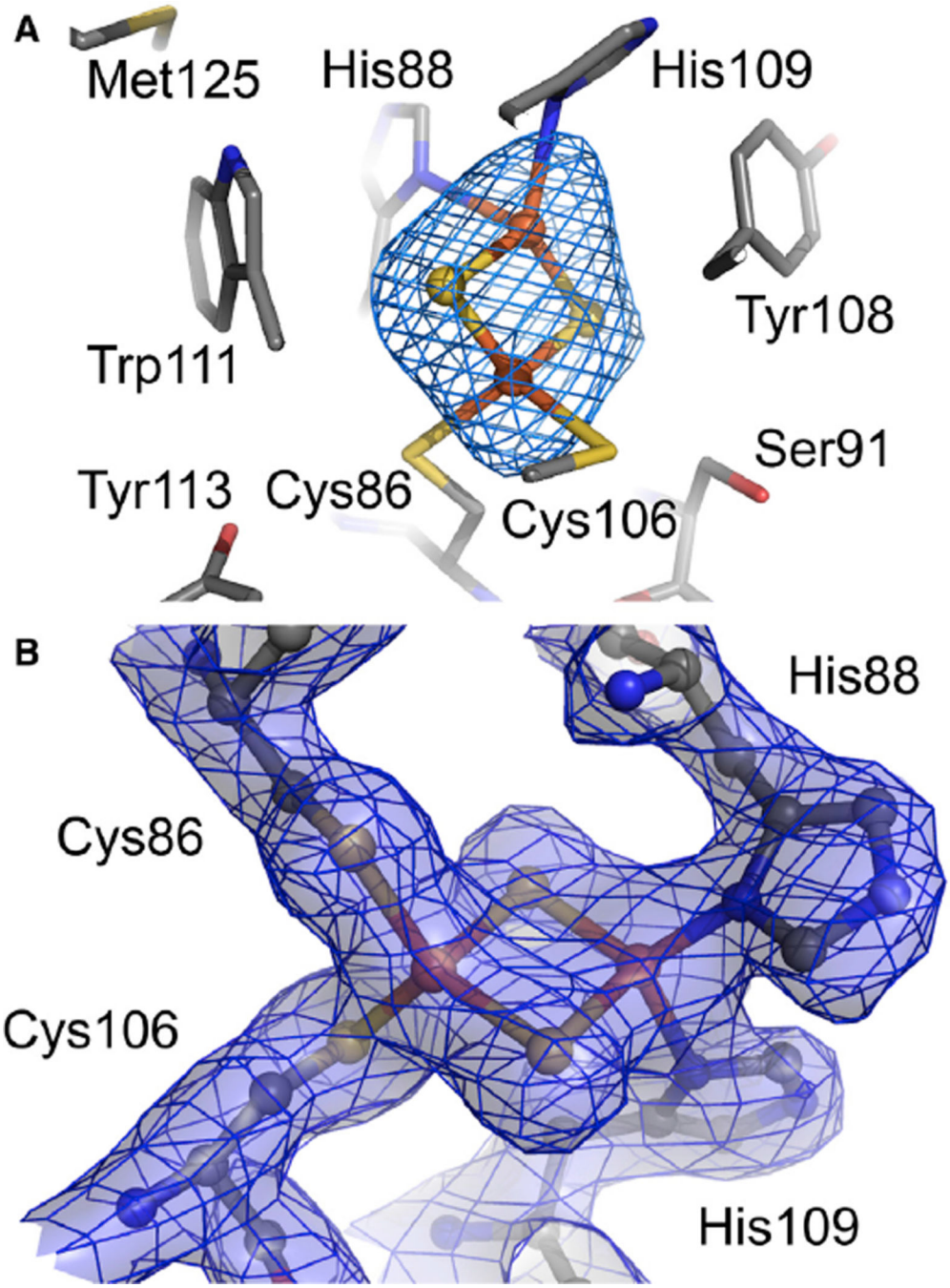

Figure 3. An Example of the Quality of the Electron Density Maps around the Rieske Cluster in the Structure of Stachydrine Demethylase

(A) The 2Fe-2S Rieske cluster within Stc2 revealed by the 3-Å resolution $F_o - F_c$ omit electron density maps contoured at +3 σ.

(B) The 2 $F_o - F_c$ map to 2.2-Å resolution is contoured at 1.5 σ and displayed as mesh with semitransparent surfaces. Atoms are colored gray, red, blue, yellow, and orange for C, O, N, S, and Fe, respectively. See also Figure S3.

Table 1

Comparison of Protein Crystal Sample Delivery Systems Used in SFX Experiments

	Flowing Sample				Fixed Target	
	Acoustic Injectors	**Electrospun Microjet**[a]	**GDVN**[b]	**LCP Injector**[c]	**Goniometer**[d]	**Si-Wafers/μ-Chips**[e]
Sample volume (μl; per data collection period)	20–70	≥25	5,100	46–100	NA[f]	1–5
Sample consumption, μg (per 1,000 X-ray pulses)	1.5	0.32	2.76	0.071	NA	NA
Crystal efficiency (crystals used per diffraction pattern)	2	1.4×10^4	2.2×10^4	>20	0.02–1	0.5–1
Crystal hit ratio with diffraction patterns observed (%)	5–50	32	4.5–50	0. 45–13	~50-100	50–100
Index ratio (%)[g]	2.7–30	0.31–50	0.8–80	3.25–85	~100	50–100
Typical XFEL frequency (Hz)	60–120+	30	60–120+	60–120+	0.1–30	10–120
Estimated average data rate (indexable diffraction data/s)	0.5–6+	3.9	0.6–2	0.4–2.1	0.1–30	0.1–~50
Crystal dimensions (μm)	5–400	1–30	0.5–20	<5	1–1000+	10–100
Chemical requirements	viscosity below ~20 cP	glycerol or PEG, electrolytes	none	LCP	oil or cryoprotectant	paratone (if not cyro-cooled)
Sample/chamber conditions (temperature and pressure)	ambient; 1 atm air or helium	ambient; <0.01 Pa or 1 atm air	ambient; <0.01 Pa or 1 atm air or helium	ambient; <0.01 Pa or 1 atm air or helium	cryogenic or ambient; 1 atm air or helium	cryogenic or ambient; 1 atm air or helium
Working distance (mm)	3–14	3–8	0.05–0.3	0.1	NA	NA

[a] Electrospun microjet information from (Kern et al., 2013; Sierra et al., 2012).

[b] GDVN data from (Boutet et al., 2012; Chapman et al., 2011).

[c] LCP injector from (Johansson et al., 2012; Kang et al., 2015; Liu et al., 2013; Weierstall et al., 2014).

[d] Goniometer data from (Cohen et al., 2014; Hirata et al., 2014; Suga et al., 2015).

[e] Si-wafers and μ-chip data from (Coquelle et al., 2015; Hunter et al., 2014; Mueller et al., 2015; Roedig et al., 2015).

[f] NA, not applicable.

[g] Percent of images considered crystal hits (>15 Bragg spots/image) and with lattices that index within anticipated space group parameters. Does not reflect images containing lattices from multiple crystals. For our acoustic injector experiments, multiple crystals were estimated to occur in less than 10% of droplets.